Pergamon

Int. J. Heat Mass Transfer. Vol. 38, No. 10, pp. 1901–1910, 1995

0017–9310/95 $9.50+0.00

0017–9310(94)00265–7

A study of thermophoretic transport in a reacting flow with application to external chemical vapor deposition processes

H. C. TSAI, R. GREIF† and S. JOH‡

Department of Mechanical Engineering, University of California at Berkeley, Berkeley, CA 94720, U.S.A.

(*Received* 10 *January* 1994 *and in final form* 2 *August* 1994)

Abstract—A study has been made of the flow, heat and mass transfer with chemical reactions and thermophoretic transport with application to external chemical vapor deposition processes. The system includes a jet that is emerging from a burner containing fuel (methane), oxygen, nitrogen and silicon tetrachloride which react and form silica soot particles. The flow impinges on a disk which serves as the target for the depositing material. The motion of the particles is determined from the combined effects of thermophoresis, buoyancy and the forced flow leaving the burner. The governing conservation equations, which include the effects of buoyancy, variable properties, chemical reactions and thermophoretic transport have been solved numerically. The effects of the burner location and the disk diameter on particle deposition are studied. The local and average particle deposition, the variation of the deposition efficiency and the heat flux are determined over a range of values of the parameters.

1. INTRODUCTION

Chemical vapor deposition processes have been successfully used for the fabrication of optical fibers [1]. In the outside vapor deposition (OVD) and vapor axial deposition (VAD) processes, silica particles are formed by passing a reacting gas/vapor stream through a high temperature flame. The gas stream and silica particles are directed towards and then deposit on a target [2–4]. Homsy *et al.* [5] and Batchelor and Shen [6] have analyzed the thermophoretic deposition of particles in a uniform flow past a cylinder based on the Blasius series solution. Garg and Jayaraj [7, 8] calculated thermophoretic deposition over a cylinder in numerical studies specifying the pressure gradient of the external flow. These studies utilized the boundary layer assumptions with simple external flows. However, experimental results [9, 10] have shown that the circumferential variation of the flow and heat transfer, as well as the interaction between the torch and the boule, have strong effects on the particle deposition. Numerical and experimental studies of particle deposition on a cylindrical target were carried out by Kim and Kim [11, 12]; deposition rates were obtained for TiO_2 particles as a function of particle diameter, flow Reynolds number and wall/gas temperature ratio at different angular position along the upstream surface of the cylinder. Kang and Greif [13] numerically investigated the thermophoretic transport for an impinging jet on a cylinder and included the effects of buoyancy, variable properties and tube rotation. Song *et al.* [14] numerically studied deposition on a cylinder for a buoyant, external variable property flow and included conduction in both the rotating cylinder and the deposited layer.

To investigate deposition for a basic configuration, experiments were carried out by Hwang and Daily [15, 16] for flame-synthesized silica particle deposition on a disk. Relevant numerical studies have been carried out by Gokoglu and Rosner [17, 18], who analyzed the thermophoretic mass transfer on a cold plate, by Alam *et al.* [19, 20], who investigated thermophoretic deposition for a plane or slot jet impinging on a flat plate, by Evans and Greif [21], who studied the flow and heat transfer in respect to a rotating disk reactor, and by Tsai and Greif [22], who studied thermophoretic transport to a disk.

Previous external deposition studies have not included the chemical reactions which produce silica [22]. This simplification contributes to the discrepancy between the numerical results and the experimental data. In the present study both methane and silicon tetrachloride oxidation are included; the silica particles are produced by silicon tetrachloride oxidation, which results from the high temperatures caused by methane oxidation. The particle laden gas flow is transported towards a disk where deposition takes place. In the analysis, single step global reaction kinetics, buoyancy and variable properties are included. A finite volume numerical method is used to discretize and solve the coupled mass, momentum, energy and species conservation equations. The detailed temperature and particle distributions are

† Author to whom correspondence should be addressed.
‡ Present address: Computational Mechanics Department, Sandia National Laboratories, Livermore, CA 94550, U.S.A.

NOMENCLATURE

A_1, A_2 pre-exponential factor
A_i convection–diffusion coefficients
b source term in the discretized equation
C mass concentration
$\bar{C}$ average mass concentration
c_p heat capacity
D diameter of the disk
D mass diffusivity
E_1, E_2 activation energy
g gravity
i, j Cartesian base vector
J local particle deposition flux
$\bar{J}$ average particle deposition flux
K coefficient of the thermophoretic velocity
k conductivity
L distance between the burner and the disk
M average molecular weight
M_i molecular weight
P thermodynamic pressure
p static pressure
Re Reynolds number $[= \rho_j \bar{u}_j D/\mu_j]$
S_ϕ source term in the discretized differential equation
T temperature
U^i gas velocity
u, v gas velocity in the x, r direction
$u_{\text{eff}}, v_{\text{eff}}$ particle velocity in the x, r direction
$u_{\text{th}}, v_{\text{th}}$ thermophoretic velocity in the x, r direction
w radius of the burner
w_c characteristic length of the Gaussian distribution
X_i mole fraction
x, r cylindrical coordinates
Y_i mass fraction.

Greek symbols
Γ general diffusivity
η deposition efficiency
μ viscosity
ν stoichiometric coefficient
ξ^i coordinates $[\xi^1 = x, \xi^2 = r]$
ρ density
τ_w shear stress at wall
ϕ general dependent variable
ω_1, ω_2 chemical reaction rate.

Superscripts
$'$ forward reaction
$''$ backward reaction.

Subscripts
N, S, E, W four nodes around the grid point P
a ambient value
j values at the burner exit
w values at the wall.

determined. Direct comparisons between the calculated and measured temperature profiles and particle deposition are made and good agreement is obtained. The uniformity and magnitude of the deposition are shown to be sensitive to the distance between the burner and the target (disk).

2. ANALYSIS

2.1. *Configuration and assumptions*

A buoyant and reacting jet flow emerges from a burner and generates silica particles in a diffusion flame; the resulting particle laden flow impinges on a disk [Fig. 1(a)]. A VAD burner is studied which was designed by Bautista *et al.* [23] and used by Hwang and Daily [15, 16]. This burner consists of eight concentric tubes, as shown in Fig. 1(b). Silicon tetrachloride and oxygen pass through the central tube, which is surrounded by a tube carrying nitrogen. Six outer tubes carry methane and oxygen, alternatively.

To analyze the phenomena the following assumptions have been made:

(1) The properties of the gas mixture vary with temperature. The thermodynamic pressure is equal to 1 atm.

(2) The flow is assumed to be laminar. The range of values of the Reynolds numbers based on the diameter of the nozzle, is from 100 to 1000, which is below the value for the onset of turbulence [24].

(3) Two irreversible reactions for methane oxidation and for silicon tetrachloride oxidation are included. The hydrolysis reaction for the silicon dioxide particles is not considered.

(4) The particle deposition mechanism has been established as resulting from thermophoresis; i.e. from the motion of a particle in a nonisothermal medium in the direction of decreasing temperature [25]. Particle deposition due to molecular diffusion is much smaller than that due to thermophoresis and is neglected [5, 6, 25, 26].

(5) The particles are smaller than one micron and the concentration is dilute; in the absence of thermophoresis, the particles would follow the gas flow [20–22].

2.2. *Governing equations*

The governing equations include chemical kinetic, fluid, energy, species and thermophoretic transport mechanisms.

1. *Chemical kinetics.* (1) Methane oxidation: meth-

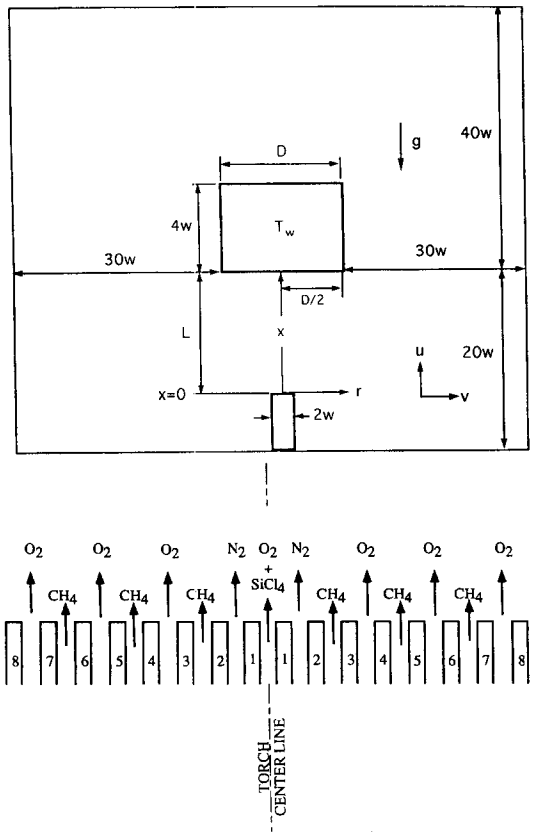

Fig. 1. (a) Configuration and computational domain. (b) Schematic diagram of the burner.

ane is utilized to generate the high temperatures needed to activate the reaction for silicon tetrachloride oxidation. Single step global reaction kinetics with an Arrhenius rate is used; the reaction rate, ω_1, given by Westbrook and Dryer [27], Westbrook [28] is

$$CH_4 + 2O_2 \rightarrow CO_2 + 2H_2O$$

$$\omega_1 = [CH_4]^{-0.3}[O_2]^{1.3} A_1 \exp\left(\frac{-E_1}{R_u T}\right).$$

The pre-exponential factor A_1 and the activation energy E_1 are equal to $8.3 \times 10^5\,\mathrm{l\,s^{-1}}$ and 30 kcal $\mathrm{mol^{-1}}$, respectively. (2) Silicon tetrachloride oxidation: this is the main mechanism that produces the silicon dioxide particles. The Arrhenius reaction rate which was used by Kim and Pratsinis [29] is given by

$$SiCl_4 + O_2 \rightarrow SiO_2 + 2Cl_2$$

$$\omega_2 = [SiCl_4] A_2 \exp\left(\frac{-E_2}{R_u T}\right).$$

Here A_2 and E_2 are equal to $1.7 \times 10^{14}\,\mathrm{l\,s^{-1}}$ and 120 kcal $\mathrm{mol^{-1}}$, respectively. The concentration of O_2 is not involved in the reaction rate for lean burning.

2. *Transport equations.* The conservation equations for mass, x-momentum, r-momentum, energy and particle concentration for the axially-symmetric round jet are written in the cylindrical coordinate system (x, r) as follows:

Continuity

$$\frac{\partial \rho}{\partial t} + \frac{\partial}{\partial x}(\rho u) + \frac{1}{r}\frac{\partial}{\partial r}(\rho r v) = 0. \quad (1)$$

The formation of the solid SiO_2 particles is neglected.

***X*-momentum equation**

$$\frac{\partial \rho u}{\partial t} + \frac{\partial \rho u u}{\partial x} + \frac{\partial r \rho v u}{r\,\partial r} = -\frac{\partial p}{\partial x} + \frac{\partial}{\partial x}\left(2\mu \frac{\partial u}{\partial x}\right) + \frac{1}{r}\frac{\partial}{\partial r}\left[r\mu\left(\frac{\partial u}{\partial r} + \frac{\partial v}{\partial x}\right)\right] - \rho g. \quad (2)$$

***R*-momentum equation**

$$\frac{\partial \rho v}{\partial t} + \frac{\partial \rho u v}{\partial x} + \frac{\partial r \rho v v}{r\,\partial r} = -\frac{\partial p}{\partial r} + \frac{\partial}{\partial x}\left[\mu\left(\frac{\partial v}{\partial x} + \frac{\partial u}{\partial r}\right)\right] + \frac{1}{r}\frac{\partial}{\partial r}\left(2r\mu \frac{\partial v}{\partial r}\right) - \frac{2\mu v}{r^2}. \quad (3)$$

Energy equation

$$\frac{\partial \rho T}{\partial t} + \frac{\partial \rho u T}{\partial x} + \frac{\partial r \rho v T}{r\,\partial r} = \frac{\partial}{c_p\,\partial x}\left(k \frac{\partial T}{\partial x}\right) + \frac{1}{c_p r}\frac{\partial}{\partial r}\left(rk \frac{\partial T}{\partial r}\right) + \sum_{k=1}^{2} \frac{\Delta H_k}{c_p} \omega_k. \quad (4)$$

The heats of combustion for CH_4 and $SiCl_4$ oxidation are included in the source term.

Gas phase species equations

$$\frac{\partial \rho Y_i}{\partial t} + \frac{\partial u \rho Y_i}{\partial x} + \frac{\partial r v \rho Y_i}{r\,\partial r} = \frac{\partial}{\partial x}\left(\rho D_i \frac{\partial Y_i}{\partial x}\right) + \frac{1}{r}\frac{\partial}{\partial r}\left(r \rho D_i \frac{\partial Y_i}{\partial r}\right) + \sum_{k=1}^{2} (v''_{ik} - v'_{ik}) \omega_k M_i, \quad i = 1, 7. \quad (5)$$

There are seven equations for $SiCl_4$, O_2, N_2, CH_4, CO_2, H_2O and Cl_2, respectively. The reaction rates for the two global reactions, ω_k $(k = 1, 2)$, are given in the previous section. M_i is the species molecular weight. The mass fraction of N_2; i.e. Y_{N_2}, is obtained by applying the relation $\Sigma_{i=1}^{7} Y_i = 1$.

SiO_2 species equation

$$\frac{\partial C}{\partial t} + \frac{\partial u_{\mathrm{eff}} C}{\partial x} + \frac{\partial r v_{\mathrm{eff}} C}{r\,\partial r} = \frac{\partial}{\partial x}\left(D \frac{\partial C}{\partial x}\right) + \frac{1}{r}\frac{\partial}{\partial r}\left(rD \frac{\partial C}{\partial r}\right) + \omega_2 M_{SiO_2} \quad (6)$$

where M_{SiO_2} denotes the molecular weight of SiO_2. The velocities of the particles equal the sum of the convective and thermophoretic velocities, i.e. $u_{\mathrm{eff}} = u + u_{\mathrm{th}}$, $v_{\mathrm{eff}} = v + v_{\mathrm{th}}$. The thermophoretic velocity is given by [30]:

$$u_{th} = -K\frac{v}{T}\frac{\partial T}{\partial x}, \quad v_{th} = -K\frac{v}{T}\frac{\partial T}{\partial r} \tag{7}$$

with K equal to 0.55 [29].

3. *Thermodynamic and transport relationships.* (1) Ideal gas law:

$$P = \rho\frac{R_u}{M}T, \quad M = \sum_{i=1}^{7} X_i M_i. \tag{8}$$

(2) Mixture properties: the properties of viscosity and conductivity are evaluated as air and vary with temperature [31]. The mass diffusivity is dependent on the temperature [32] and is evaluated by assuming binary diffusion between the individual species and air.

2.3. *Boundary and initial conditions*

1. Burner: the gases pass through eight concentric tubes [Fig. 1(a)] and the flow rates are specified in Table 1 [15].

2. Solid surfaces include the disk and the burner walls: the velocities are zero on the solid surfaces. The temperature of the disk is equal to 1300 K ($= T_w$). The burner walls are insulated. The boundary conditions for concentration, mass fraction are $\partial(C, Y_i)/\partial n = 0$, where n is the direction normal to the solid surface.

3. Open boundaries: the second derivative of the variable in the normal direction is set equal to zero at the unconfined boundary. This is validated by numerical tests and is discussed in a later section.

2.4. *Deposition flux and deposition efficiency*

The local particle deposition flux, $J(x = L, r) \equiv J(r)$, is equal to the product of the axial component of the thermophoretic velocity, $u_{th,w}$, and the particle mass concentration, C_w, at the wall:

$$J(x = L, r) \equiv J(r) = u_{th,w}C_w. \tag{9}$$

The average particle deposition flux, $\bar{J}(x = L) \equiv \bar{J}$, is given by

$$\bar{J}(x = L) \equiv \bar{J} = \frac{8}{D^2}\int_0^{D/2} u_{th,w}C_w r\,dr \tag{10}$$

where D is the diameter of the disk.

The deposition efficiency η is defined as the ratio of the total deposition rate, $\bar{J}\pi D^2/4$, to the equivalent mass flow rate of SiO_2, which is determined stoichiometrically from the inlet mass flow rate of $SiCl_4$ and is given by

$$\eta = \frac{\displaystyle\int_0^{D/2} Jr\,dr}{\displaystyle\int_0^{w_1} u_j(0,r)\rho Y_1(0,r)r\,dr}\frac{M_{SiCl_4}}{M_{SiO_2}} = \frac{\bar{J}D^2}{8\displaystyle\int_0^{w_1} u_j(0,r)\rho Y_1(0,r)r\,dr}\frac{M_{SiCl_4}}{M_{SiO_2}} \tag{11}$$

where w_1 is the radius of the central tube where $SiCl_4$ flows, u_j is the velocity at the burner exit and Y_1 is the mass fraction of $SiCl_4$.

3. NUMERICAL METHOD

3.1. *Numerical procedure*

The governing equations (1)–(6) were written in conservative form and discretized in time using the backward Euler method, i.e. a first-order implicit method. To minimize oscillations resulting from higher order schemes, the HYBRID scheme is adopted [33], which linearizes the convective terms for moderate Reynolds numbers. A central difference representation is used for the diffusion terms. Due to the highly nonlinear nature of the reaction terms they are treated explicitly in both the energy and species equations. This minimizes oscillations while solving the elliptical system [34].

The linkage between the continuity and momentum equations, i.e. the determination of the pressure, proceeds according to the SIMPLE algorithm of Patankar [33] by making corrections at each iteration, until the velocities and the corrected pressure field satisfy the coupled continuity and momentum equations. A non-staggered grid system is chosen; all dependent variables are calculated and stored at the same intersection of grid lines rather than at staggered grid locations. To minimize difficulties with the determination of the pressure field, the velocities (on the surfaces of the control volume) are determined differently; i.e. they are obtained by solving linearized momentum equations [35]. The implicitly imposed boundary conditions for the pressure correction equation are given by the components of the momentum equations which are normal to the boundary surfaces [36].

To solve the discretized linear equations, the generalized minimum residual method (GMRES) [37] with incomplete lower and upper triangle matrix decomposition (ILU) preconditioning is adopted because of its robustness and fast convergence. The criterion used for convergence is that the sum of the dimensionless residuals over the entire domain is less than 10^{-5} for every equation. In addition, it is also required that the relative change of each dependent variable is less than 0.01% for each iteration. The time step used in the present problems is equal to 0.001 s. The steady state is achieved by marching a sufficient time to ensure that the solution is subjected to change that is less than 0.1% in successive time steps.

3.2. *Validation, computational domain and grid dependency*

The numerical code extended the authors' previous work [22] and was validated using several benchmark tests. Methane oxidation is the dominant reaction and it is necessary to examine the highly nonlinear behavior resulting from this reaction. The finite rate reaction term for methane oxidation is validated in the

following section. Referring to Fig. 1(a), the upstream and downstream locations are fixed at $-20w$ and $+40w$, respectively, and the lateral region extends from $-30w-D/2$ and $+30w+D/2$. The results for the skin friction coefficient and Nusselt number change by less than 1% if the dimensions of the domain are increased by 20%. The length and diameter of the burner, and the length of the disk, are $9w$, $2w$ and $4w$, respectively. The burner is centered on the target and the distance between the burner exit and the target is $8.7w$.

Fine grids are employed in the regions near the burner and the target to resolve the sharp temperature and concentration gradients. The finest grid is 0.005 w ($w = 1.58$ cm). Moderately fine grids are used in the regions surrounding the disk to resolve the large gradients and the recirculation regions. Typical grids in (x, r) coordinates were 141×151 for disk diameters equal or less than 6 cm, which was checked to ensure grid-independent results. For the case $D = 6$ cm and $\phi = 0.6$, increasing the grids to 141×171 changed the local shear stress and heat fluxes by 0.1 and 0.07%, respectively. By decreasing the grids to 121×151, both results changed by 0.5%. Further decreasing the grids to 121×121, both results changed by 0.1 and 0.1%, respectively. Changing the grids to 141×121, the local shear stress and heat flux on the wall changed by 1.0 and 0.9%, respectively. For the larger disk ($D = 7.5$ and 9 cm), more grids, typically 141×201, were utilized.

4. RESULTS AND DISCUSSION

4.1. *Comparison with the experimental data of Hwang and Daily* [15, 16]

The simulations for particle deposition shown in Fig. 1(a), (b) are based on the system of Hwang and Daily [15, 16]. Temperature profiles in their free vertical VAD jet were measured in methane diffusion flame experiments in the absence of silica. Numerical and experimental results for the temperature profiles are presented in Fig. 2(a), (b) for equivalence ratios, ϕ, equal to 0.25 and 0.4 (the flow rates in each ring are given in Table 1). The area-averaged velocity of the jet at the burner exit, $\bar{u}_j$, is obtained from the inlet flow rates in each ring and is calculated to be 3.0 and 3.5 m s^{-1} for $\phi = 0.25$ and 0.4, respectively. Radial temperature distributions at three axial distances, $x = 2.8$, 7.6 and 12.5 cm, are presented. The highest temperatures occur near the burner exit (in the region away from the centerline) due to the oxidation of methane in this region. The temperature along the center line is low because the methane is flowing in the outer rings [Fig. 1(b)] and the heat released from the reaction slowly diffuses inward. The result is that the temperatures in the region away from the center decrease downstream, while the temperatures near the center increase downstream. The leaner case, $\phi = 0.25$, results in a lower center temperature than the case $\phi = 0.4$. In general, there is good agreement

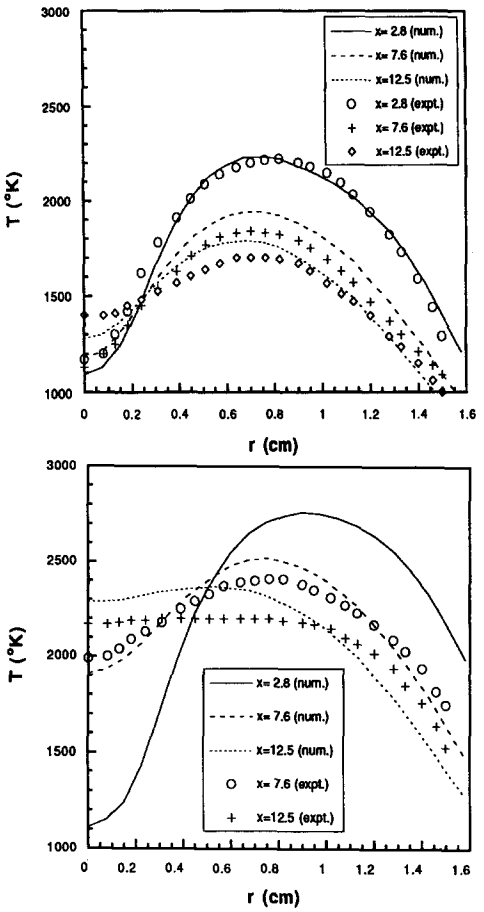

Fig. 2. (a) Radial temperature distributions in the CH_4 oxidation free jet at $x = 2.8$, 7.6, 12.5 cm; $\phi = 0.25$. (b) Radial temperature distributions in the CH_4 oxidation free jet at $x = 2.8$, 7.6, 12.5 cm; $\phi = 0.4$.

for the shape and the magnitude of the temperature distributions; the uncertainty of the temperature measurement was ± 80 K [15].

Two chemical reactions are included in the particle deposition calculations, i.e. methane and silicon tetrachloride oxidation. The global equivalence ratio for the methane oxidation reaction is 0.6 and $SiCl_4$ is flowing in the central tube at a mass flow rate of 3 g min^{-1}. Calculations were carried out for a diameter of the burner, $2w$, of 3.125 cm; the temperature of the disk, T_w, was 1300 K; the thickness of the disk was 6 cm; the diameter of the disk, D, was varied from 4.5 to 9 cm; the area-averaged velocity of the jet at the burner exit, $\bar{u}_j$, was 2.8 m s^{-1}; and the Reynolds number, Re ($= \rho_j \bar{u}_j D/\mu_j$), varied from 266 to 533. The experiments were carried out for a fixed distance between the exit of the burner and the disk, L, of 13 cm; calculations were made for a range of values of L from 6.25 to 26 cm.

The velocity vectors and the isothermal contours are shown in Figs. 3(a), (b) and 4(a), (b) for $D = 6$ and 9 cm ($Re = 355$, 533) and $L = 13$ cm. The buoyant jet may be considered to include free jet, stagnation, wall jet, near and far wake regions. The upstream region

Table 1. Distribution of the flow in the burner

Ring no.	Inside diameter [mm]	Outside diameter [mm]	Gas delivered	$\phi = 0.25$ [l min^{-1}]	$\phi = 0.4$ [l min^{-1}]	$\phi = 0.6$ [l min^{-1}]	[g min^{-1}]
1	3.34	4.76	O_2 or $SiCl_4$	2.9 (O_2)	2.9 (O_2)	1.22 (O_2)	3 ($SiCl_4$)
2	6.53	7.96	N_2	4	4	5.49	
3	10.21	12.7	CH_4	0.33	1.23	0.33	
4	16.06	17.46	O_2	7.6	7.6	6.39	
5	20.45	22.23	CH_4	1.08	1.53	1.98	
6	24.38	25.4	O_2	7.4	7.4	4.81	
7	27.56	28.58	CH_4	1.71	2.15	2.6	
8	31.62	34.93	O_2	7.35	7.35	4.38	

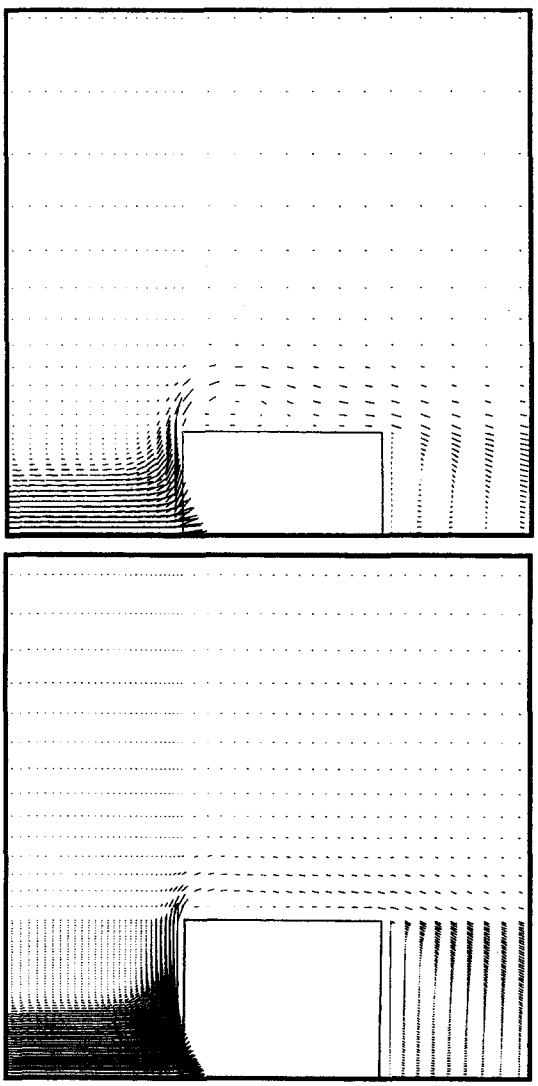

Fig. 3. (a) Velocity vectors in the x–r plane; $D = 6$ cm, $L = 13$ cm, $Re = 380$. (b) Velocity vectors in the x–r plane; $D = 9$ cm, $L = 13$ cm, $Re = 570$.

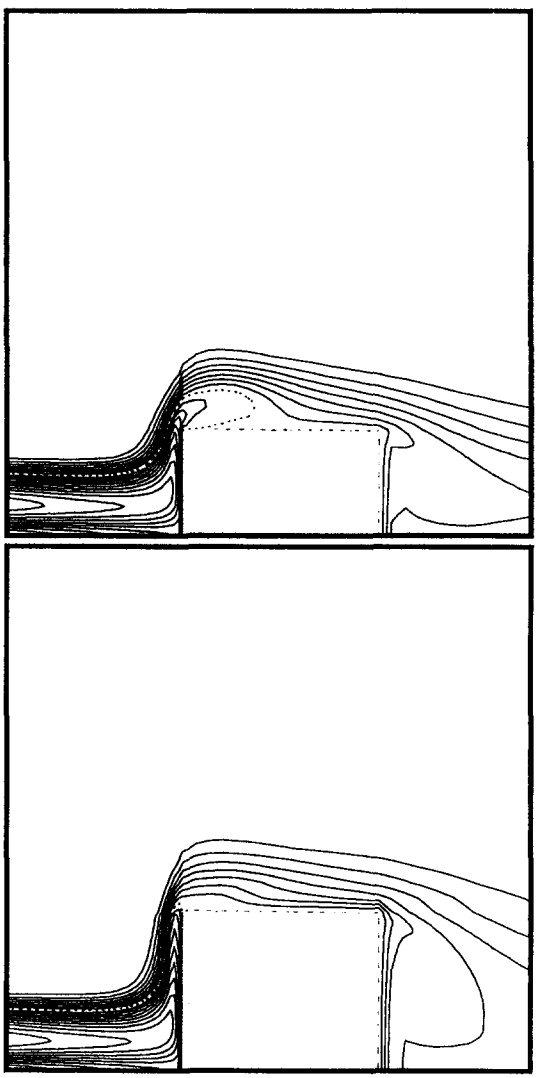

Fig. 4. (a) Isothermal contours in the x–r plane; $D = 6$ cm, $L = 13$ cm, $Re = 380$. (b) Isothermal contours in the x–r plane; $D = 9$ cm, $L = 13$ cm, $Re = 570$.

essentially corresponds to a developing free jet with a small pressure gradient; the flow impinges on the disk and separates upon turning around the disk. Recirculation occurs along the sides and rear of the disk.

The temperature distribution for $\phi = 0.6$, $D = 6$ cm, $L = 13$ cm, is shown in Fig. 5. For the three equivalence ratios studied, the maximum temperatures occur in the outer regions and are greatest for

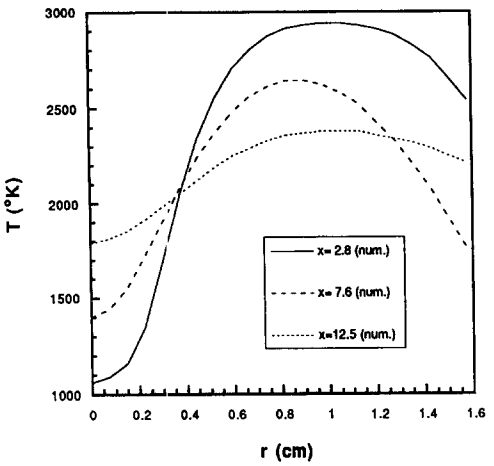

Fig. 5. Radial temperature distributions in the CH_4 oxidation free jet at $x = 2.8$, 7.6, 12.5 cm; $\phi = 0.6$.

$\phi = 0.6$ and occurs at $x = 2.8$ cm. [It is pointed out that in the central region the temperatures are higher for $\phi = 0.4$, Fig. 2(b), than for $\phi = 0.6$, because for the $\phi = 0.4$ case, Table 1, there is much more CH_4 flowing in ring number 3 which is close to the center.] In respect to the production of silica particles it is pointed out that the oxidation of $SiCl_4$, which occurs near the center [see the VAD torch, Fig. 1(b)], requires high temperatures to initiate the reaction.

The temperature contours marked by the dashed curves shown in Fig. 4(a), (b) are equal to the temperature of the disk. Near the front surface of the disk the gas temperatures are much higher than the surface temperature and large temperature gradients are present; this results in large thermophoretic forces. The maximum heat and deposition fluxes occur away from the stagnation point [Fig. 6(a), (b)], because the methane reaction occurs at the outer rings; this differs from the non-reacting jet results [22]. The radial distribution of the SiO_2 mass concentration at the wall is shown in Fig. 6(a).

The radial distributions of the $SiCl_4$ and SiO_2 mass concentrations are shown in Fig. 7(a) at three axial locations, $x = 2.8$, 7.6 and 12.5 cm. The axial variations of $SiCl_4$ and SiO_2 at the center line are shown in Fig. 7(b). $SiCl_4$ and O_2 are premixed and flowing in the central ring; the high temperatures surrounding the central ring are approx. 2000 K (see Fig. 5; note that the outer diameter of ring 1 is 0.476 cm). The reaction of $SiCl_4$ produces SiO_2 (silica particles); near the jet exit, e.g. at $x = 2.8$ cm, the maximum particle concentration occurs at $r = 0.4$ cm [Fig. 7(a)], which is outside both the central and the second rings. Further downstream the particle concentration increases and the location of the maximum concentration shifts toward the center. Note that the maximum concentration of $SiCl_4$ is at the center and its value decreases downstream.

The radial variations of the deposition flux, $J(r)$, the heat flux, $q(r)$, and the silica concentration at the disk $[C_w(r)]$ are shown in Fig. 6(a) and (b). The

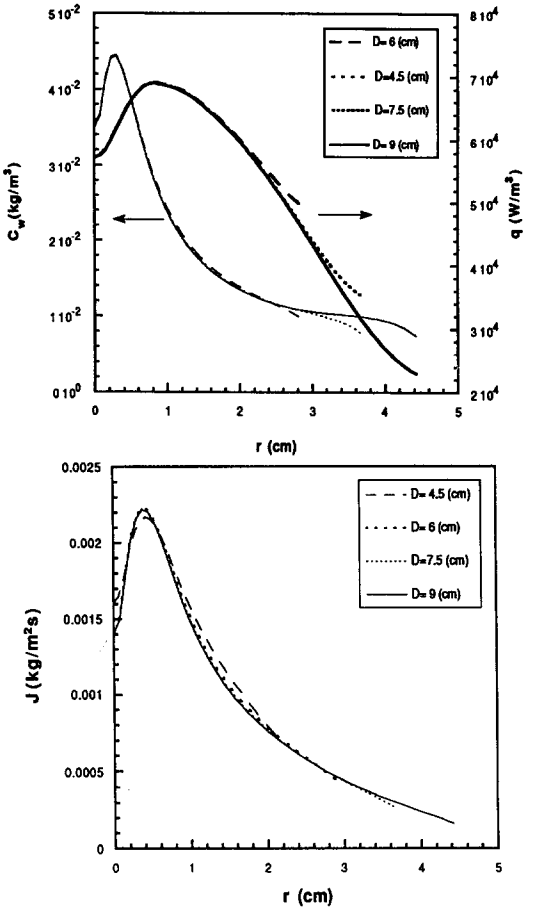

Fig. 6. (a) Variation of the particle concentration and the heat flux along the surface, effect of D; $L = 13$ cm. (b) Variation of the particle deposition flux along the surface, effect of D; $L = 13$ cm.

deposition flux, $J(r)$, is proportional to $C_w(r)u_{th,w}(r)$ or $C_w(r)q(r)$ [equation (7)]; both $u_{th,w}$ and q are proportional to the temperature gradient normal to the disk surface (note that the temperature of the disk is constant). Recall that, for a uniform constant property flow impinging on an infinite disk, the fluxes are constant along the surface. For the present conditions, the radial distributions are variable and (non-monotonic) and are essentially independent of the size of the disk. Therefore, the total deposition rate, $\int J2\pi r\,dr = \bar{J}\pi D^2/4$, increases with increasing diameter over the range of diameters and conditions studied. [For very large disks, $J(r) \to 0$ at large radii, and the total deposition rate would then be constant for increasing values of the disk diameter.]

The experimental data of Hwang [16] and the present calculations for the variation of the total particle deposition rate, $\bar{J}\pi D^2/4$, with respect to disk diameter, are shown in Fig. 8. The profiles of the two results are in excellent agreement, but the calculations exceed the data by an almost constant value of 20%. Note that the deposition efficiency, η, is proportional to the total particle deposition rate.

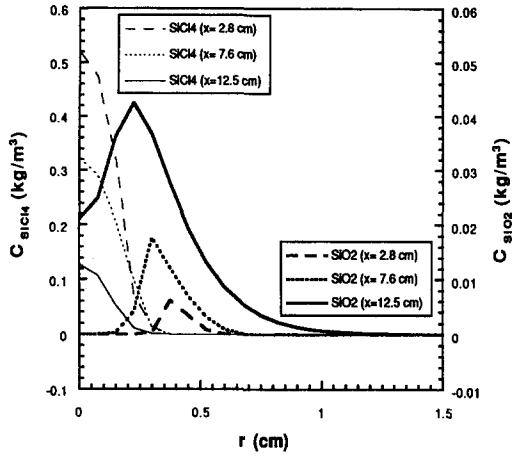

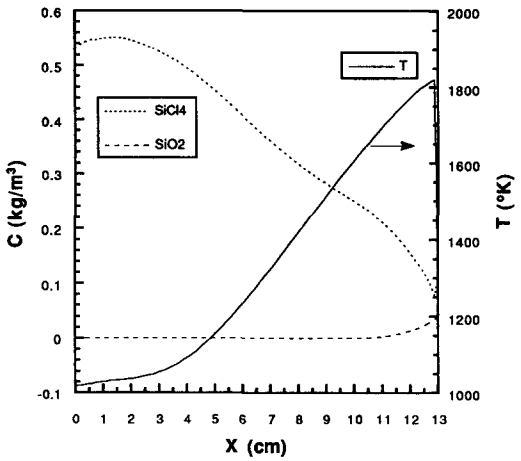

Fig. 7. (a) Radial variation of $SiCl_4$ and SiO_2 concentrations at $x = 2.8, 7.6, 12.5$ cm; $D = 6$ cm, $L = 13$ cm. (b) Variation of the concentrations of SCl_4 and SiO_2 and the temperature along the center-line; $D = 6$ cm, $L = 13$ cm.

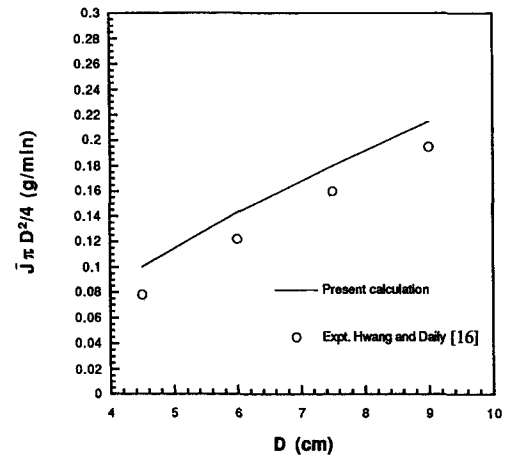

Fig. 8. Variation of the total deposition rate with disk diameter; $L = 13$ cm.

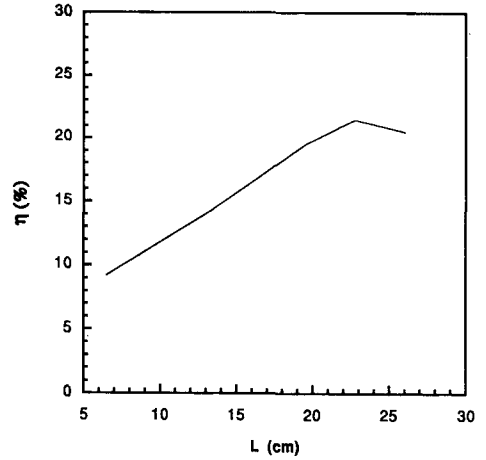

Fig. 9. Variation of the deposition efficiency with separation distance; $D = 6$ cm.

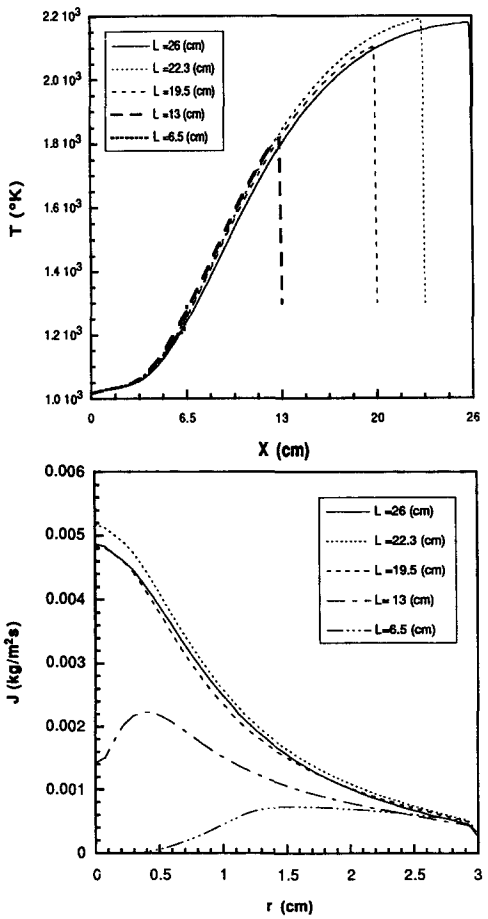

Fig. 10. (a) Variation of the temperature along the centerline, effect of L; $D = 6$ cm. (b) Variation of the deposition flux along the surface, effect of L; $D = 6$ cm.

4.2. *Effect of distance between burner and target*, L

In Fig. 9 it is seen that, over the range of separation distances studied (6.5 cm $< L <$ 26 cm), the deposition efficiency for $D = 6$ cm varies significantly with L. For $L < 23$ cm, the deposition rate increases as the separation distance increases; for $L = 6.5$ cm the efficiency is 9% and for $L = 22.3$ cm the efficiency is 22%. The temperature distributions along the center line [$T(x, r = 0)$, Fig. 10(a)] show that, for $L < 23$ cm,

increasing L yields increasing values of the temperature. This indicates that the chemical heat released from the CH_4 reaction is continuing to diffuse to the center line. Over the range $L < 23$ cm, the chemical heat release and diffusion dominate over the cooling effect of the expanding jet; for increasing L (but still for $L < 23$ cm) the longer time for the flow to reach the target permits more heat to diffuse to the center line (the lower temperature zone) and more SiO_2 particles are produced. For $L < 23$ cm the deposition flux increases for increasing L [Fig. 10(b)] and the efficiency increases (Fig. 9). It is also noted that increasing L results in more particle deposition near the central region [Fig. 10(b)].

For $L > 23$ cm, the deposition efficiency (Fig. 9) and the deposition flux [Fig. 10(b)] decrease slightly as the separation distance L increases. The larger separation distance (e.g. $L = 26$ cm) results in a lower center-line temperature than for $L = 22.3$ cm [Fig. 10(a)], which produces a smaller temperature gradient (and a smaller thermophoretic force) near the target surface. In addition, for the larger distances L the lateral spreading of the jet and the particles results in a greater number of particles that do not impinge on the target. Therefore, for $L > 23$ cm, these effects result in a smaller deposition efficiency for increasing L.

5. CONCLUSIONS

The equations of mass, momentum, energy and species, including the effects of chemical reactions, thermophoresis, variable properties and buoyancy have been solved numerically to predict the fluid flow, heat transfer and particle deposition on a disk. The following conclusions are drawn:

(1) The present numerical simulation is in good agreement with the temperature profiles obtained in the methane diffusion flame experiments of Hwang and Daily [15].

(2) The shape of the curve for the calculated deposition rate with respect to disk diameter is in excellent agreement with the experimental data of Hwang [16], but the numerical values exceed the data by an almost constant value of 20%.

(3) The distance between the burner and the target, L, is an important parameter in determining the silica particle deposition distribution and the efficiency. For $L < 23$ cm, the deposition efficiency increases as L increases; however, for $23 < L < 26$ cm, the deposition efficiency decreases slightly for increasing L.

(4) Detailed calculations were made for a distance between the burner and the target, L, of 13 cm and the resulting radial distribution of the deposition flux is non-monotonic and essentially independent of the size of the target.

Acknowledgements—Support from the National Science Foundation and the Pittsburgh Supercomputer Center is gratefully acknowledged. The research is part of a joint program with Professor J. W. Daily of the University of Colorado on chemical vapor deposition processes. The authors are indebted to Professors J. W. Daily, A. C. Fernandez-Pello and J. Hwang for helpful discussions.

REFERENCES

1. T. Li, *Optical Fiber Communications*: Vol. 1. *Fiber Fabrication*. Academic Press, London (1985).
2. P. C. Schultz, Fabrication of optical waveguides by the outside vapor deposition process, *Proc. IEEE* **68,** 1187 (1980).
3. A. M. Morrow, A. Sarkar and P. C. Schultz, Outside vapor deposition. In *Optical Fiber Communications*: Vol. 1. *Fiber Fabrication* (Edited by T. Li). Academic Press, London (1985).
4. N. Niizeki, N. Inagaki and T. Edahiro, Vapor-phase axial deposition method. In *Optical Fiber Communications*: Vol. 1. *Fiber Fabrication* (Edited by T. Li). Academic Press, London (1985).
5. G. M. Homsy, K. L. Walker and F. T. Geyling, Blasius series for thermophoretic deposition of small particles, *J. Colloid Interface Sci.* **83,** 495–510 (1981).
6. G. K. Batchelor and C. Shen, Thermophoretic deposition of particles in gas flowing over cold surfaces, *J. Colloid Interface Sci.* **107,** 21–37 (1985).
7. V. K. Garg and S. Jayaraj, Thermophoretic deposition over a cylinder, *Int. J. Engng Fluid Mech.* **3,** 175–196 (1990).
8. V. K. Garg and S. Jayaraj, Thermophoretic deposition in crossflow over a cylinder, *J. Thermophys.* **4,** 115–116 (1990).
9. J. R. Bautista, K. L. Walker and R. M. Atkins, Modeling heat and mass transfer in optical waveguide manufacturing, *Chem. Engng Proc.* 47–52 (1990).
10. G. M. Graham and M. K. Alam, Experimental study of the outside vapor deposition process, *Aerosol Sci. Technol.* **15,** 69–76 (1991).
11. Y. J. Kim and S. S. Kim, Numerical simulation of particle deposition onto a circular cylinder in non-isothermal two-phase cross flows. *ASME/JSME Therm. Engng Proc.* **2,** 95–100 (1991).
12. Y. J. Kim and S. S. Kim, Experimental study of particle deposition onto a circular cylinder in high-temperature particle-laden flows, *Expl Therm. Sci.* **5,** 116–123 (1992).
13. S. H. Kang and R. Greif, Thermophoretic transport in the outside vapor deposition process, *Int. J. Heat Mass Transfer* **36,** 1007–1018 (1993).
14. Y. Song, M. Choi and S. H. Kang, A study of heat transfer and particle deposition during the outside vapor deposition process, *The 6th International Symposium on Transport Phenomena*, Vol. 4, pp. 199–204 (1993).
15. J. Hwang and J. Daily, Characterization of a vapor axial deposition (VAD) flame impinging on a disk for a study of electric field enhanced deposition, *Expl Therm. Fluid Sci.* **8,** 58–66 (1994).
16. J. Hwang, Flame deposition processes in materials manufacturing, Ph.D. Dissertation, University of California, Berkeley, CA (1991).
17. S. A. Gokoglu and D. E. Rosner, Viscous dissipation effects on thermophoretically augmented aerosol particle transport across laminar boundary layers, *Int. J. Heat Fluid Flow* **6,** 293–297 (1985).
18. S. A. Gokoglu and D. E. Rosner, Thermophoretically augmented mass transfer rates to solid walls across laminar boundary layers, *AIAA J.* **24,** 172–179 (1986).
19. M. K. Alam, G. Graham, V. Janakiraman and J. Greaves, Numerical analysis of thermophoretic transport in the OVD process, HTD-Vol. 130, *Numer. Heat Transfer* (ASME) **HTD-130,** 67–72 (1990).
20. M. K. Alam, G. Graham and V. Janakiraman, Particle transport by thermophoresis in a slot jet impinging on a wall, *Heat Transfer Eff. Mater. Proc.* (ASME) **HTD-233,** 15–21 (1992).

21. G. Evans and R. Greif, A numerical model of the flow and heat transfer in a rotating disk chemical vapor deposition reactor, *ASME J. Heat Transfer* **109,** 1063–1069 (1986).
22. H. C. Tsai and R. Greif, Thermophoretic transport with application to external vapor deposition processes, *Int. J. Heat Mass Transfer* **37,** 257–268 (1994).
23. J. R. Bautista, E. Potkay and D. L. Scatton, Particle size measurement in optical waveguide manufacturing torches using light scattering, *Mater. Res. Soc. Symp. Proc.* **117,** 151–156 (1988).
24. H. Tennekes and J. L. Lumley, *A First Course in Turbulence*. MIT Press, Cambridge, MA (1972).
25. P. G. Simpkins, S. G. Kosinski and J. B. MacChesney, Thermophoresis: the mass transfer mechanism in modified chemical vapor deposition, *J. Appl. Phys.* **50,** 5676–5681 (1979).
26. K. L. Walker, G. M. Homsy and F. T. Geyling, Thermophoretic deposition of small particles in laminar tube flow, *J. Colloid Interface Sci.* **69,** 138–147 (1979).
27. C. K. Westbrook and F. L. Dryer, Simplified reaction mechanisms for the oxidation of hydrocarbon fuels in flames, *Combust. Sci. Technol.* **27,** 31–43 (1981).
28. C. K. Westbrook, Personal communication (1993).
29. K. S. Kim and S. E. Pratsinis, Manufacture of optical waveguide preforms by modified chemical vapor deposition, *A.I.Ch.E. Jl* **34,** 912–920 (1988).
30. L. Talbot, R. K. Cheng, R. W. Schefer and D. R. Willis, Thermophoresis of particles in a heated boundary layer, *J. Fluid Mech.* **101,** 737–758 (1980).
31. T. Cebeci and P. Bradshaw, *Physical and Computational Aspects of Convective Heat Transfer*. Springer, New York (1984).
32. R. B. Bird, W. E. Stewart and E. N. Lightfoot, *Transport Phenomena*. Wiley, New York (1960).
33. S. V. Patankar, *Numerical Heat Transfer and Fluid Flow*. Hemisphere, New York (1980).
34. C. P. Mao, A. C. Fernandez-Pello and J. A. C. Humphrey, An investigation of steady wall ceiling and partial enclosure fires. *J. Heat Transfer* **106,** 221 (1984).
35. M. J. Schuh, Numerical prediction of fluid and particle motions in flows past tubes, Ph.D. Dissertation, University of California, Berkeley, CA (1987).
36. P. M. Gresho and R. L. Sani, On pressure boundary condition for the incompressible Navier–Stokes equations, *Int. J. Numer. Meth. Fluids* **7,** 1111–1145 (1987).
37. Y. Saad and M. H. Schultz, GMRES: a generalized minimal residual algorithm for solving nonsymmetric linear systems, *SIAM J. Sci. Stat. Comput.* **7,** 856–869 (1986).